

Triboelectric Programmed Droplet Manipulation for Plug-and-Play Assembly

Roujuan Li, Xiang Li, Zhiwei Zhang, Morten Willatzen, Zhong Lin Wang,* and Di Wei*

Programmed droplet transport which is typically directed by surface energy gradients or external fields, is crucial in domains ranging from chemical reaction modulation to self-powered intelligent sensing. However, droplet motion control remains constrained by path reconfiguration, requirements on chemical surface modification, and platform complexity. Here, a more universal plug-and-play droplet manipulation paradigm based on liquid-solid contact electrification and triboelectric wetting on common dielectric surfaces is reported. By regulating the electrical double layer via asymmetric ion dynamics, the triboelectric charge polarity of droplets can be adjusted, enabling in situ manipulation without path reconfiguration dictated by the conventional droplet motion output. Droplets achieved an ultrahigh velocity of 450 mm s^{-1} on general surfaces, significantly exceeding the speeds observed in droplets subjected to constant electrostatic fields with chemical modifications. This flexible and modular functionally decoupled manipulation strategy offers an environmentally friendly, cost-effective, and versatile paradigm, facilitating applications in chemical analysis and smart sensing.

liquid-solid (L-S) interfacial energy. Among these external fields, the electric field has emerged as a powerful driving force for droplet transport, due to its simplicity and scalability.^[25] Particularly, the electrowetting on dielectric (EWOD)^[26–28] with rapid response and high erasability has attracted considerable attention. Although means of external stimulus input have been developed, such as the manipulation of droplets employing electrostatic induction induced by triboelectric fields, which eliminates additional energy constraints from external electric fields.^[29–32] However, there are still several limitations, including the complexity of the manipulation platform and frequent path reconfiguration and frequent path reconfiguration.^[33]

Conventional electrical-based droplet manipulation strategies utilize circuits or electrodes that couple both the energy supply and actuation roles, leading to reduced

flexibility and increased complexity of the manipulation platform. Furthermore, these methods heavily rely on repetitive path reconfiguration to achieve control of droplet motion behavior, which makes it challenging to flexibly modify droplet motion behavior without readjusting surface structures and electrostatic fields. Additionally, past efforts have often required advanced chemical modification of the surface if a high level of droplet control is to be achieved. However, chemical modifications using reagents such as perfluorosilane inevitably faced environmental impacts and difficulties in recycling. Overcoming the constraints of the necessity of path reconfiguration and achieving efficient droplet motion control on general surfaces and simple platforms poses a significant challenge.

1. Introduction

Programmable manipulated droplets can serve as an outstanding carrier for energy and information flow, which is significant in harvesting water,^[1–5] heat transfer,^[6,7] energy scavenging,^[8–10] chemical analysis,^[11,12] printing process,^[13–15] and clinical diagnostics,^[16,17] etc. The widespread applicability of these techniques depends on the precision of droplet control on surfaces. To achieve efficient droplet control, methods such as introducing energy gradients on the substrate or applying asymmetric forces via external electrical,^[18–20] thermal,^[21] optical,^[22] and magnetic^[23,24] fields are employed. Despite the diversity of methods, the underlying mechanism lies in the regulation of

R. Li, X. Li, Z. Zhang, M. Willatzen, Z. L. Wang, D. Wei
Beijing Institute of Nanoenergy and Nanosystems
Chinese Academy of Sciences
Beijing 101400, China
E-mail: zhong.wang@mse.gatech.edu; weidi@binn.cas.cn

R. Li, X. Li, Z. Zhang
School of Nanoscience and Engineering
University of Chinese Academy of Sciences
Beijing 100049, China

Z. L. Wang
Guangzhou Institute of Blue Energy
Knowledge City
Huangpu District, Guangzhou 510555, China

Z. L. Wang
Beijing Key Laboratory of Micro-Nano Energy and Sensor
Center for High-Entropy Energy and Systems
Beijing Institute of Nanoenergy and Nanosystems
Chinese Academy of Sciences
Beijing 101400, China

D. Wei
Centre for Photonic Devices and Sensors
University of Cambridge
9 JJ Thomson Avenue, Cambridge CB3 0FA, UK

The ORCID identification number(s) for the author(s) of this article can be found under <https://doi.org/10.1002/adfm.202416457>

DOI: 10.1002/adfm.202416457

Here, a ubiquitous plug-and-play droplet manipulation paradigm based on triboelectrification and triboelectric-wetting on dielectric was proposed to dynamic control droplet motion on general surfaces. It combined solid-solid contact electrification (SS-CE) and liquid-solid contact electrification (LS-CE)^[25,34–37] to consider the impact of droplet charging properties on electrowetting and droplet manipulation from the perspective of electrical double layer (EDL) for the first time. First, the impact of the asymmetry between anions and cations in ionic liquids on CE with dielectric materials was examined. It was discovered that asymmetric ions caused different EDL structures at the L-S interface, directly influencing the polarity of the droplet's triboelectric charge and thereby dynamically controlling its motion behavior. Compared to the conventional EWOD method, the droplet manipulation strategy based on EDL regulation demonstrated superior collective performance, eliminating the need for programmed path reconfiguration, reducing surface and energy constraints, and enhancing antigravity capability and flexibility. This strategy enabled remote and in situ motion control from the droplet's perspective, removing the necessity for frequent pre-defined paths according to motion output requirements. Additionally, an ultrahigh average velocity of 450 mm s⁻¹ was achieved on common dielectric surfaces without chemical modifications, guided by the self-powered triboelectric field. Here, only small areas of physical modifications were utilized that were more environmentally friendly. Notably, the modular manipulation strategy exhibited functional decoupling properties, simplifying platform complexity. The plug-and-play design facilitated seamless integration and customization of diverse functional modules, obviating complicated installation and commissioning. This versatile strategy is applicable in ion concentration detection, chemical reaction modulation, and ionic logic circuit control. The dynamic regulation of the EDL, integrated with the plug-and-play design for droplet control, constitutes a novel paradigm for programmed manipulation, offering substantial potential for chemical analysis and self-powered intelligent sensing.

2. Results and Discussion

2.1. Plug-and-play Triboelectric Droplet Manipulation

To achieve controlled droplet motion on polymer surfaces, previous studies predominantly concentrated on surface engineering.^[38,39] However, the intrinsic properties of the droplets, along with their triboelectric impact, are frequently overlooked. In this work, a flexible plug-and-play approach based on CE and triboelectric-wetting was developed to facilitate efficient manipulation of droplet motion behavior (Movie S1, Supporting Information). Triboelectricity can offer a cost-effective and environmentally friendly method for droplet manipulation.^[25,40–42] As shown in Figure S1 and Movie S2 (Supporting Information), a straightforward triboelectric field could attract droplets to move along a specific path. As shown in Figure 1a, the plug-and-play design consisted of two main modules: the pre-charged module and the functional module. The red dashed area refers to the pre-charged module, the blue dashed area refers to the functional module examples, and the black dashed area refers to the final realized applications

examples. The pre-charged module generated a controlled triboelectric charge on the droplet via LS-CE. The functional module established a triboelectric field via SS-CE between two dielectric materials with markedly different electronegativities. The modular manipulation strategy effectively decoupled the pre-charging and driving functions of the droplets. The plug-and-play approach enabled customization for diverse applications, including droplet actuation, sorting, and detection, among others. These two modules were simply linked by physical contact, facilitating the tunable triboelectric droplet manipulation. The detailed model is illustrated in Figure 1b, showcasing the pre-charged module and the functional module, which comprises the micrometer-sized pillar region and the triboelectric field region. First, polytetrafluoroethylene (PTFE) films (15 cm × 10 cm) were adhered to acrylic plates as the solid contact layers within both modules. Subsequently, to improve the flexibility of manipulating droplet movement, a micrometer-sized pillar region was designed on the PTFE surface within the functional module using an engraving machine. Scanning electron microscope images and 3D profiles of the laser-etched PTFE portion were captured, revealing pillar dimensions of 100 μm diameter (Figures S2 and S3, Supporting Information). The application of laser etching resulted in a notable enhancement of surface roughness and an increase in the hydrophobicity of the substrate. Following laser etching, the static contact angle (CA) of water on PTFE increased from 106° to 136° (Figure S4, Supporting Information). Energy dispersive spectroscopy revealed that laser etching hardly changed the PTFE surface composition (Figure S5, Supporting Information). However, the etched PTFE became brittle, so the etching was confined to the vicinity of the droplet landing point on the functional module (2 cm width). This approach preserved functionality while minimizing surface processing complexity. Finally, the triboelectric field generated by SS-CE was constructed on the PTFE surface within the triboelectric field region, positioned next to the micrometer-sized pillar region. The droplet underwent LS-CE with the PTFE within the pre-charged module, resulting in the triboelectric charges of a specific polarity. Subsequently, the droplet landed on the functional module, driven by the triboelectric field generated by the SS-CE between fur and PTFE. As shown in Figure S6 (Supporting Information), the process of rubbing PTFE and fur was in horizontal sliding mode. When PTFE and fur came in touch, the electrons were transferred from fur to PTFE due to the stronger attraction of PTFE to the electrons. At the end of the 10 cycles, the PTFE and fur separate with the charges remaining on their respective surfaces, leaving a negative triboelectric field on the PTFE. It generated a surface potential^[43] that could be measured by an electrostatic voltmeter. At this time, the potential of the PTFE surface basically reached saturation at ≈3000 V. Rubbing with fur was faster and more flexible than traditional EWOD in that it eliminated the cumbersome arrangement of power circuits and electrode structures, making it a more environmentally friendly and cost-effective means. The surface triboelectric field could be considered substantially uniform due to the extensive rubbing of a large fur piece across multiple cycles. To elucidate the surface potential of the functional module exhibiting a negative triboelectric field, potential measurements were conducted at five designated locations using an electrostatic voltmeter, with the results detailed in Figure S7 (Supporting

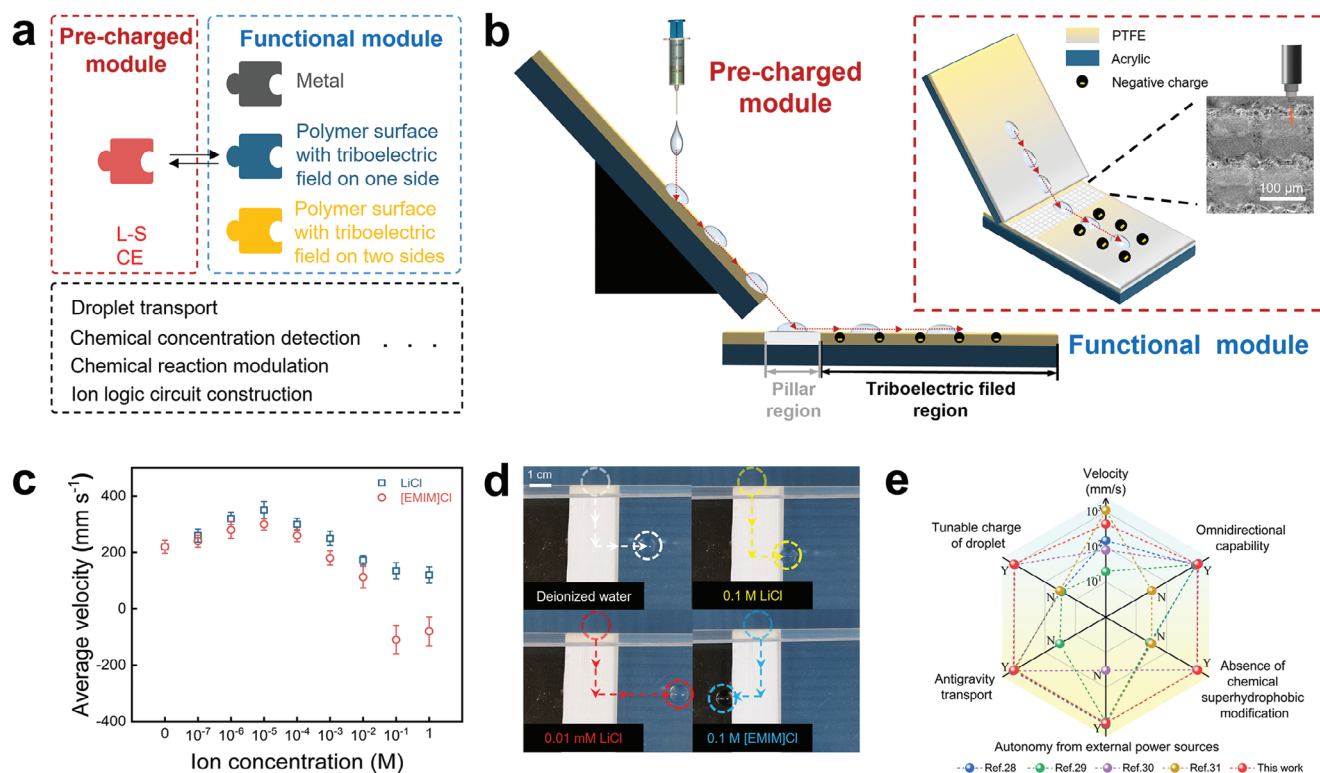


Figure 1. Plug-and-play triboelectric droplet manipulation. a) Schematic diagrams showed that Plug-and-play was usually assembled from two basic modules (pre-charged, functional module). b) Schematic detail of the modular droplet manipulation device. c) The average velocity of movement of LiCl and [EMIM]Cl droplets of different concentrations on the surface of a negative triboelectric field. The error bars were standard error values of three tests. d) Deionized water, 10^{-5} M LiCl, 0.1 M LiCl, and 0.1 M [EMIM]Cl droplets could be classified according to their direction of motion and distance. e) Comparison of our work with previously reported electrically based droplet manipulation from six perspectives (velocity, omnidirectional capability, absence of chemical superhydrophobic modification, autonomy from external power sources, antigravity transport, and tunable charge of droplet). “Y” and “N” denoted Yes and No, respectively.

Information). It suggests that, owing to the near-saturation of the surface charge, the potential distribution remained approximately uniform (≈ -3000 V), thereby minimizing any influence on droplet driving performance.

To validate the impact of the triboelectric charge of droplets on its motion behavior, LiCl and 1-Ethyl-3-methylimidazolium Chloride ([EMIM]Cl) droplets of different concentrations (each with a volume of $10\ \mu\text{L}$) were slid from the pre-charged module to the functional module with a negative triboelectric field. Before each experiment, an ion blower was used for 60 s to eliminate residual surface charges. The fur and PTFE were rubbed the same number of times in all experiments to ensure the same triboelectric field. The final distance travelled and the average velocity of the droplets on the functional module are shown in Figure S8 (Supporting Information) and Figure 1c. Different droplets were observed to exhibit distinct motion behaviors. Among them, the 10^{-5} M LiCl droplet traveled the longest distance and had the highest average velocity. The efficient transport of the droplet on an inclined surface was further demonstrated, wherein the droplet defied gravitational forces and ascended a 30° incline propelled by electrostatic attraction (Figure S9 and Movie S3, Supporting Information). To represent the 2D control of the droplet by this strategy, an arc-shaped triboelectric field was constructed on the functional module. After a $10\ \mu\text{L}$ 10^{-5} M LiCl droplet was

released from the pre-charged module, it was observed that the droplet moved in an arc-shaped path on the functional module (Figure S10, Supporting Information). It further demonstrated the excellent performance of the strategy and provided new ideas for future applications in digital microfluidics. Additionally, a reversal of direction was observed in the movement of 0.1 and 1 M [EMIM]Cl droplets. This reversal might be attributed to the disparity in triboelectric charge polarity arising from the distinct EDL structures at the interface between the droplet and the pre-charged module. Droplet sorting was significantly enhanced when triboelectric field regions of opposite polarity were constructed on both sides of the micrometer-sized pillar region on the functional module. Specifically, a positive triboelectric field was generated by a nylon film rubbed with silk, while a negative triboelectric field was induced by PTFE rubbed with fur. To enhance the consistency of the positive and negative triboelectric field regions within the functional module, a total of 10 rubbing cycles with fur and PTFE were performed for the negative triboelectric field region, yielding a measured PTFE surface potential of ≈ 3000 V. For the positive triboelectric field region, 20 rubbing cycles with nylon and silk were conducted, resulting in a nylon surface potential of ≈ 3000 V as measured by an electrostatic voltmeter. Deionized water, 10^{-5} M LiCl, 0.1 M LiCl, and 0.1 M [EMIM]Cl droplets could be classified according to their direction

and distance of motion, as shown in Figure 1d. It is noteworthy that while the positive and negative triboelectric field regions may exhibit irregularities with identical rubbing cycles, the overall direction of the triboelectric field remains consistent. It has minimal impact on the sorting results, further demonstrating the versatility of the method. As depicted in Figure 1e, the performance of this study was compared with previously reported electrically based droplet manipulation in six key perspectives: velocity, omnidirectional capability, absence of chemical superhydrophobic modification, autonomy from external power sources, antigravity transport, and tunable charge of the droplet. Overall, our droplet manipulation strategy demonstrated superior collective performance compared to other similar methods in terms of antigravity capability, flexibility, and reduced surface and energy constraints. Instead of frequent path reconfiguration for diverse motion outputs, in situ droplet motion control was truly achieved by leveraging the dynamic regulation of the EDL. Notably, it achieved a maximum average velocity of 450 mm s^{-1} , multiple-fold higher than the speeds observed in droplets subjected to constant electrostatic fields with chemical modifications.

2.2. Mechanism of Droplet Triboelectric Charge Controlled by EDL Regulation

EDL serves as the fundamental mechanism for triboelectric charge generation in droplets via LS-CE.^[44,45] Furthermore, to regulate the triboelectric charge generated by the droplets in the pre-charged module, the impact of ion type on the EDL at the L-S interface was examined. Specifically, solutions of LiCl (characterized by minimal size disparity between its cation and anion) and room temperature ionic liquid [EMIM]Cl (featuring an asymmetric cation-anion pair) were selected to explore the effect of asymmetry in anions and cations on the CE of dielectric materials. The experimental setup is illustrated in Figure 2a. A $15 \text{ cm} \times 10 \text{ cm}$ PTFE film was mounted on an acrylic substrate at a 45° angle of inclination. The syringe pump, grounded via a syringe, consistently dispensed a droplet of $\approx 10 \mu\text{L}$ onto the PTFE surface. The triboelectric charge carried by the droplet was measured as it slid through the PTFE into the Faraday cylinder. The release height of the droplet, sliding distance, and droplet volume were kept constant in all experiments. As shown in Figure 2b and Figure 2c, LiCl droplets of varying concentrations consistently produced positive triboelectric charges upon sliding off the PTFE surface. In contrast, the charge polarity of [EMIM]Cl droplets transitioned from positive to negative as the concentration increased. The mechanism underlying droplets carrying diverse triboelectric charges might be attributed to structural disparities in the EDL at the L-S interface. In stage I (S I), characterized by ultra-low ion concentrations (Figure 2d i), the charge generated by the deionized water droplet was only $\approx 0.32 \text{ nC}$. This limited charge generation is likely due to insufficient ion concentration, which cannot fully support ion transfer at the L-S interface.^[46] The slight increase in ion concentration in stage II (S II) resulted in a greater amount of transferred charge being measured. The measured transfer charge reached the maximum (0.53 nC) when the concentration of the LiCl droplet was increased to 10^{-5} M , offering a superior option for subsequent experiments. This could be attributed to the enhanced conduc-

tivity of the liquid, which facilitates the ion transfer process, thereby forming a more compact inner Helmholtz plane (IHP) (Figure 2dii). With further increase in ion concentration to stage III (S III), the triboelectric charge of the droplet gradually decreased and eventually converged to zero. This might be caused by the shielding effect of the EDL, which interferes with the electron transfer process (Figure 2diii). It should be noted that the highest concentration for S III of the [EMIM]Cl droplets was just 10^{-2} M . Stage IV (S IV) emerged as the concentration increased to 0.1 M or higher, under which condition, the triboelectric polarity of the [EMIM]Cl droplet was reversed to become negative, with a triboelectric charge of $\approx 0.11 \text{ nC}$ for a 0.1 M [EMMIM]Cl droplet. This polarity reversal of the droplets at high concentrations might result from a different EDL structure induced by a large quantity of asymmetric ions. This phenomenon might be related to the hydrophobicity of [EMIM]⁺^[47] (Note S1, Supporting Information), whereby the presence of asymmetric ions affects the stable arrangement of the EDL due to complex and unbalanced repulsive forces. As shown in Figure S11 (Supporting Information), the same inversion phenomenon also occurred in other ionic solutions with an asymmetric cation-anion pair, such as lithium bis(trifluoromethanesulfonyl)imide (Li[TFSI]). Therefore, it does not imply that a particular ion was contained to complete the control but rather focused more on the difference in charge transfer due to variations in the structure of the EDL. The results demonstrated that symmetric ions might not cause charge reversal, whereas high concentrations of asymmetric ions were more inclined to do so. This was an effective way to control the amount and polarity of the charge carried on the droplets by regulating the EDL. Besides changing the ionic concentration of the droplets, different solid friction materials could play the same regulatory role due to differences in material electronegativity. As shown in Figure S12 (Supporting Information), $10 \mu\text{L}$ of 10^{-5} M LiCl droplets were released from the same height onto PTFE and nylon surfaces, respectively. After sliding down at the same distance, the droplets after contact with PTFE were measured to be positively charged ($\approx 0.53 \text{ nC}$), while those with nylon film were negatively charged ($\approx 0.08 \text{ nC}$). It further demonstrated the flexibility and adaptability of this modulation strategy, thus laying the foundation for programmable droplet manipulation.

2.3. Performance Characterization of Droplet Manipulation

When droplets fell on the pillar region, the Coulomb force exerted on the droplet by the negative triboelectric field on the functional module could be quantified by the following equation:

$$F_C = \oint T_{ij} \cdot ndS, \text{ with } T_{ij} = \epsilon_0 \left(E_i E_j - \frac{\delta_{ij}}{2} E^2 \right), i, j = x, y \quad (1)$$

where T_e , \mathbf{n} , ϵ_0 , δ_{ij} , and E are the Maxwell stress tensor, the surface unit normal, the permittivity of air, the Kronecker delta function, and the magnitude of the triboelectric field intensity, respectively. The distribution of T_e on the droplet was calculated through a finite element analysis using COMSOL Multiphysics (version 6.2). The lateral component of T_e , $T_{e,x}$, was concentrated on the front surface and the rear surface of droplets. The component was larger on the front surface of a positively charged droplet

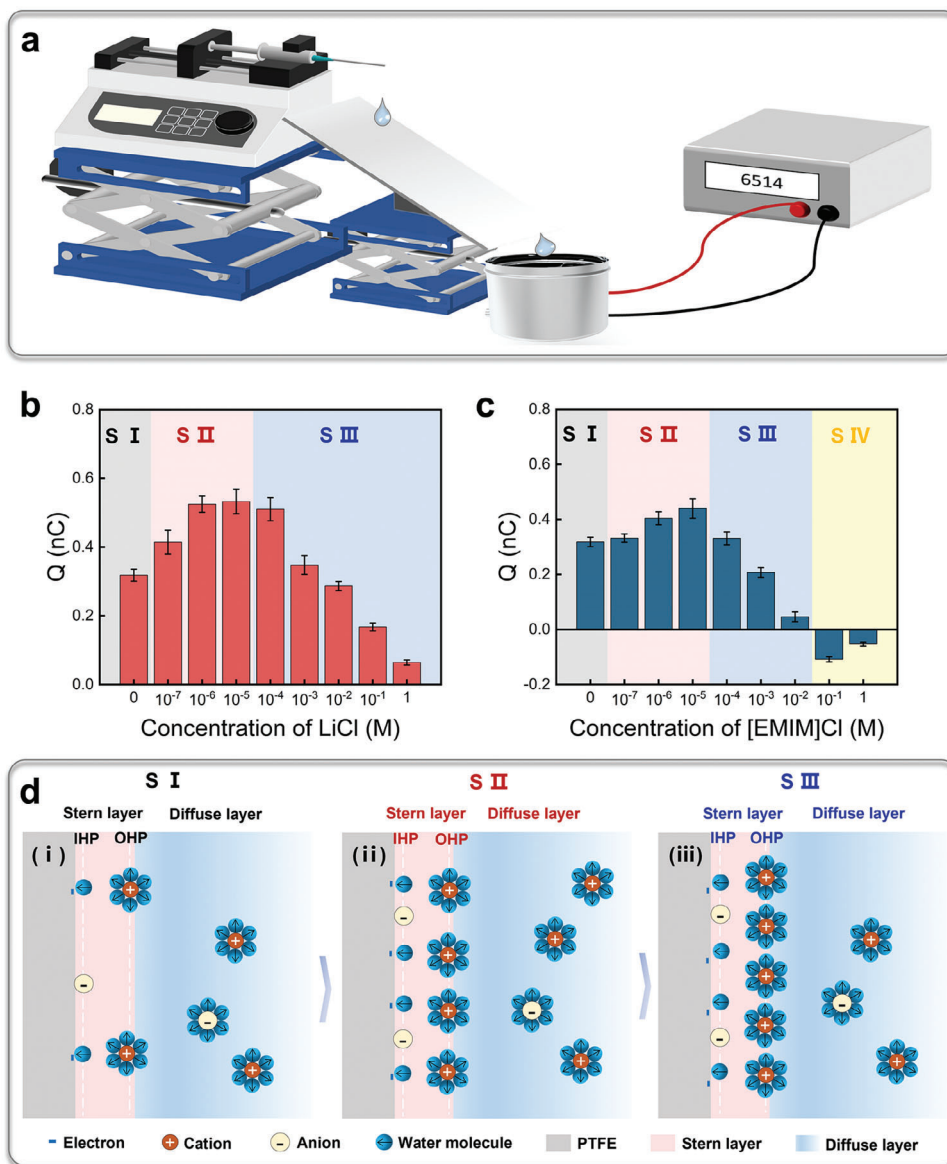


Figure 2. Droplet triboelectric charge controlled by EDL regulation. a) Experimental setup diagram for measuring the triboelectric charge of the droplets. b) Triboelectric charges measured in LiCl solutions of different concentrations. c) Triboelectric charges measured in [EMIM]Cl solution of different concentrations. d) Mechanism of formation of the EDL at the CE interface between droplets and PTFE film. (i) EDL structure for stage I. (ii) EDL structure for stage II. (iii) EDL structure for stage III.

(Figure S13a, Supporting Information) whereas that of the back surface of a negatively charged droplet was higher (Figure S13b, Supporting Information), which was consistent with the direction of the droplet's motion. The driving force F_{Cx} acting on the droplet could be obtained by integration of the numerically calculated $T_{e,x}$ over the droplet surface. Due to electrostatic attraction, the positively charged droplet overcame the lateral adhesion force F_d , resulting in an acceleration toward the side of the negative triboelectric field (Figure S14a and Note S2, Supporting Information). Conversely, negatively charged droplets moved away from the negative triboelectric field due to electrostatic repulsion (Figure S14b, Supporting Information). For positively charged droplets, the negative triboelectric field reduced the interfacial

energy between the droplet and the solid surface, thus promoting the wetting of the droplet to the solid surface. As the positive charge of the droplet was neutralised and EWOD occurred, the droplet moved for a distance and finally stopped in the negative triboelectric field region. The potential distribution generated during the whole movement is shown in Figure 3a. The specific length parameters of PTFE were set the same as shown in Figure 1b. The charge density of PTFE is $5 \times 10^{-7} \text{ C m}^{-2}$. The droplet size was $10 \mu\text{L}$, and the charge was set according to the experimentally obtained droplet-carrying charge, respectively. Taking a water droplet as an example, the CA on PTFE decreased to 95° when the motion ceased (Figure S15, Supporting Information), confirming the occurrence of triboelectric-wetting on

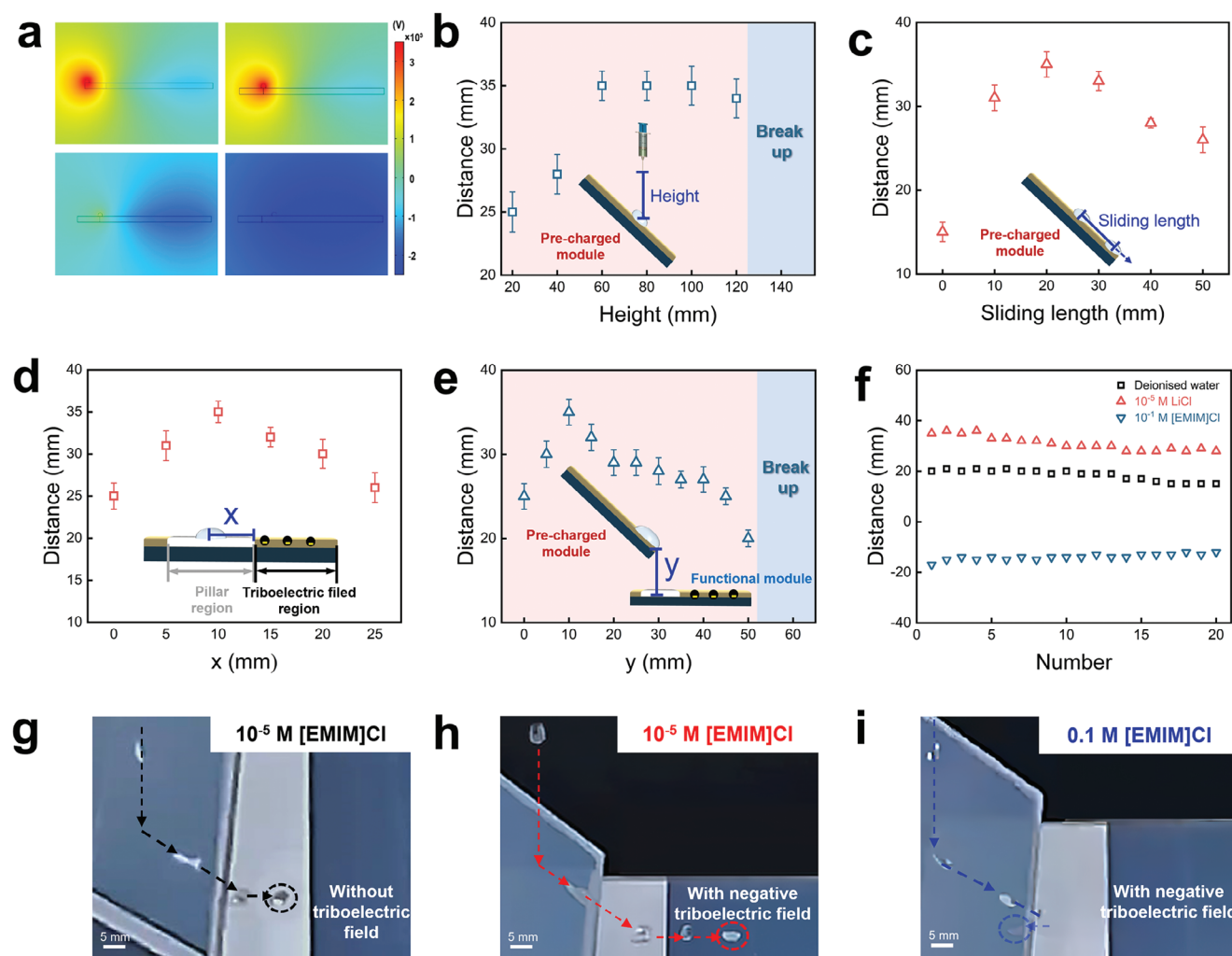


Figure 3. Performance characterization of droplet manipulation. a) Simulation of the surface potential distribution of PTFE during droplet motion. b) Effect of droplet release height on the pre-charged module on its motion distance on the functional module. c) Effect of droplet sliding length on the pre-charged module on its motion distance on the functional module. d) Effect of the length between the droplet's landing point in the micrometer-sized pillar region and the triboelectric field region on its motion distance. e) Effect of the height from the functional module surface to the horizontal plane of the pre-charged module edge on droplet motion distance. f) Property changes of droplet motion after driving 20 droplets consecutively. g) A 10^{-5} M [EMIM]Cl droplet was slid from the pre-charged module to the functional module with no triboelectric field. h) A 10^{-5} M [EMIM]Cl droplet was slid from the pre-charged module to the functional module with a negative triboelectric field. i) A 0.1 M [EMIM]Cl droplet was slid from the pre-charged module to the functional module with a negative triboelectric field. The error bars in a, b, d, and e were standard error values of three tests.

dielectric. The final distance of the droplet movement could be calculated based on the conservation of energy to simplify the analysis of droplet dynamics. (details of the calculation process can be found in Note S2, Supporting Information). The droplet could be considered as a point charge and the rubbed PTFE could be considered as a uniformly charged body. Theoretical calculations indicated that the movement distance of a droplet was correlated with its charged quantity and polarity, which was consistent with the conclusions in our experiments. The theoretical calculation and practical results of the final motion distance of droplets with different concentrations of LiCl and [EMIM]Cl are shown in Figure S16 (Supporting Information). The theoretical and experimental results were found to be in good agreement, validating the control of droplet motion distance by the CE process.

To further explore the impact of factors such as droplet release height and sliding length on the pre-charged module for controlled motion, 10^{-5} M LiCl droplets capable of carrying the maximum transferred charge were selected for the experiments. First, droplets were released onto the pre-charged module from various heights. As shown in Figure 3b, the final motion distance of the droplet on the functional module initially increased with height, reaching optimal performance at 60 mm. Beyond this height, the motion distance no longer increased significantly. Droplet breakup was observed when the release height exceeded 120 mm, which was detrimental to droplet transport and manipulation. This trend was influenced by the triboelectric charge generated in the pre-charged module (Figure S17a, Supporting Information). The same trend was observed in the average velocity of

the droplets (Figure S17b, Supporting Information). This was the effect of the difference in initial potential energy causing a change in the initial velocity of the droplet as it left the pre-charged module in conjunction with the triboelectric charge. 60 mm was chosen as the optimal release height of the droplet on the pre-charged module to obtain the maximum average velocity. Next, the sliding distance of the droplet on the pre-charged module was gradually increased while maintaining a constant release height. A similar upward trend was observed when the sliding length of the droplet on the pre-charged module was less than 30 mm, attributed to the increasing adequacy of triboelectrification (Figure 3c). After a sliding length of more than 30 mm, the distance over which the droplets were driven on the functional module gradually decreased. This reduction was due to a decrease in droplet charge resulting from loss of adhesion (Figure S17c, Supporting Information). Therefore, 30 mm was picked as the optimal sliding length of the droplet on the pre-charged module. The tilt angle of the substrate simultaneously affects both the velocity and direction of the droplet when it falls from the pre-charged module. A tilt angle of 45° was identified as the optimum angle (Figure S17d, Supporting Information). Moreover, investigations were undertaken to explore the influence of diverse droplet volumes on the propulsion of droplet movement. Droplet volume also exerted discernible effects on both propulsion velocity and displacement, and 10 μ L droplets were selected (Figure S18, Supporting Information). As shown in Figure S19 (Supporting Information), droplets with volumes ranging from hundreds of nanoliters to several hundred microliters could be manipulated. It showed excellent performance over a wide volume range, and the same level in the past often required thousands of volts of high pressure to achieve. It is undeniable that CE-induced wetting^[48] occurred throughout the droplet manipulation process. However, this minor effect could be neglected in the presence of a strongly triboelectric field.

Plug-and-play assembly emphasized the importance of connectivity between modules. The 10⁻⁵ M LiCl droplets were utilized to investigate the effect of the connection parameters of the two modules on the droplet motion performance. As shown in Figure 3d, *x* presents the length between the droplet's landing point in the micrometer-sized pillar region and the triboelectric field region. As the droplet moved across the micrometer-sized pillar region, it continued to accumulate charge, enhancing the electrostatic attraction. However, when the droplet was positioned too far from the triboelectric field region, electrostatic attraction could not occur. Consequently, the longest propulsion distance could be obtained when *x* = 10 mm. Similarly, as shown in Figure 3e, *y* denoted the height from the functional module surface to the horizontal plane of the pre-charged module edge. When *y* was too low, the droplet fell onto the functional module with a small initial velocity and could not be driven a long distance. When *y* exceeded 50 mm, the droplets tended to break up. It turned out that when *y* = 10 mm, the droplets exhibited the longest propulsion distance. To verify the impact of humidity on the surface triboelectric field, experiments were carried out with 10⁻⁵ M LiCl droplets. As shown in Figure S20 (Supporting Information), the triboelectric field depended on the air humidity. The surface potential of PTFE decreased at high humidity, and the velocity and distance of movement of the droplets were also reduced. This might be attributed to the fact that high-humidity

air in contact with PTFE forms EDL, which might play a shielding role against the surface triboelectric field. Therefore, low air humidity was beneficial in maintaining the desired droplet manipulation. After selecting the optimal parameters, deionized water, 10⁻⁵ M LiCl, and 0.1 M [EMIM]Cl droplets were consecutively driven to demonstrate the stability and repeatability of the plug-and-play triboelectric droplet manipulation at least 20 times. It could be observed that there was no significant deterioration in droplet motion performance (Figure 3f). It further exhibits the simplicity and cost-effectiveness of the strategy. Additionally, reproducible surface triboelectricity on functional modules enabled erasability for droplet manipulation (Figure S21, Supporting Information).

To display the manipulation of droplet motion behavior by EDL regulation, high-speed videos from side-view were captured to observe the process of electrostatic attraction and repulsion. In the first case, there was no triboelectric field being constructed on the functional module. A 10⁻⁵ M [EMIM]Cl droplet experienced minimal movement due to the influence of inertia after sliding from the pre-charged module (Figure 3g; Movie S4, Supporting Information). In the second scenario, a 10⁻⁵ M [EMIM]Cl droplet was slid from the pre-charged module to the functional module with a negative triboelectric field. Figure 3h demonstrated that this droplet was propelled to move a significantly longer distance than the previous one. In the third case, a 0.1 M [EMIM]Cl droplet underwent the same process as in the second case. In contrast, the droplet moved away from the negatively charged surface under the influence of electrostatic repulsion (Figure 3i). All of the aforementioned phenomena validate the manipulation of droplet motion behavior by regulating the EDL. Besides the ion concentration and type, the external triboelectric field also exhibited the capability to remotely and dynamically regulate the EDL, thereby manipulating droplet motion (Movie S5, Supporting Information). The 10⁻⁵ M LiCl droplets were used to study the influence of the external triboelectric field on the triboelectric charge and the motion distance of the droplets. A nylon film rubbed with silk was pasted on the back side of the pre-charged module to generate an external positive triboelectric field. The gradual enhancement of the triboelectric field was achieved with increased rubbing cycles, resulting in a corresponding rise in the triboelectric charge of the droplets and a longer motion distance (Figure S22a, Supporting Information). Conversely, a PTFE film with a negative triboelectric field after rubbing with the fur was adhered to the back side of the pre-charged module, resulting in a decrease in the positive charge of the droplets. The triboelectric charge of the droplets reversed polarity under the strong triboelectric field. It was observed that the motion distance and direction of the droplets exhibited the same tendency as that of the charge (Figure S22b, Supporting Information). This effect of dynamic modulation of EDL is likely due to the positive triboelectric field facilitating electron transfer from water molecules to the PTFE surface via electrostatic induction and also attracting more anions to adsorb on the film surface, whereas the negative triboelectric field attracting cations in the droplets to the vicinity of the film surface.^[49] With triboelectric field modulation, a maximum transport velocity of 450 mm s⁻¹ was achieved when transporting a 10 μ L droplet of 10⁻⁵ M LiCl, significantly surpassing the speed of droplets under constant electrostatic fields. As shown in Figure S23 (Supporting Information), changes in the shape of the

trailing edge of the droplets at high velocities are due to gigantic contact line friction based on standard fluid dynamics.^[50,51] Besides the variation of droplet concentration and external remote triboelectric field, adjusting the surface electric field strength through the number of rubbing cycles of fur with PTFE or silk with nylon allows for control over the droplet's movement distance. Specifically, the cycle numbers for both positive and negative triboelectric fields were systematically increased from 1 to 10 while utilizing 10^{-5} M LiCl droplets. The results indicated a proportional increase in the motion distance of the droplets with the increasing rubbing cycle numbers (Figure S24, Supporting Information).

2.4. Triboelectric Droplet Manipulation and its Applications

The plug-and-play design facilitated diverse applications for droplet motion, utilizing triboelectrification to regulate charge or ion signal output in the pre-charged module, and the functional module could be customized for tasks such as chemical concentration detection, chemical reaction regulation, and logic circuit construction. Chemical concentration detection is essential for industrial applications, ecology, and physiological health. Efficient chemical concentration detection was performed when the pre-charged module was combined with a functional module covering aluminum (Al) film, as shown in Figure 4a. The concentration of sulphate and chloride is common and important for production and life. Consequently, Na_2SO_4 and NaCl droplets were chosen for the experiments, respectively. As shown in Figure 4b,c, there was a significant correlation between the current signals collected by the Al film and the droplet concentration. Typically, the current decreased with increasing ion concentration when the concentration exceeded 0.01 M. This suggested that the strategy could function as threshold sensing to detect the ion concentration range based on the triboelectric signals. For Na_2SO_4 droplets, the current at a concentration of 0.01 M was ≈ 10 μA . If the measured current was below this value, the droplet might be considered to have a high sulfate concentration higher than 10 μA . Similarly, a 0.01 M NaCl droplet exhibited a current signal of ≈ 12 μA , which could serve as a threshold for detecting chloride. This technique rapidly discriminated between deionized, tap, and drinking water, based on distinct current signals induced by variations in SO_4^{2-} and Cl^- anion concentrations (Figure S25, Supporting Information). It established a foundation for more sophisticated ion concentration detection, which is favorable for future development and research at lower differentiation steps in the next stages. In addition, voltage signals (Figure S26, Supporting Information) also demonstrated the capability to detect varying concentrations of Na_2SO_4 and NaCl. This strategy has major implications for the fields of chemical analysis and smart sensing. It is also worthwhile to be convinced that this strategy offers ideas for the future introduction of new technologies for sensing applications such as water quality monitoring. When the functional module consists of the micrometer-sized pillar region and the negative triboelectric field region constructed on the PTFE film, the 10^{-7} M, 10^{-6} M, and 10^{-5} M NaCl droplets obtained different movement distances after sliding down from the pre-charged module, as shown in Figure S27 (Supporting Information). This might have potential

applications for targeted drug delivery by precisely controlling the delivery distance.

Chemical reaction modulation enhances reaction efficiencies and reduces both laboratory and industrial costs. The plug-and-play droplet manipulation paradigm enabled droplet transport and sorting simultaneously, improving the selectivity of chemical reactions. As shown in Figure 4d, the functional module was divided into two parts by the micrometer-sized pillar region, where the left triboelectric field region was positively charged and the right triboelectric field region was negatively charged. The pre-charged module regulated the charge polarity of the droplets, directing them to move in different directions. The images in Figure 4e demonstrated the capability of droplets to act as reactors and facilitate chemical reactions. Two purple litmus droplets were placed in the positive triboelectric field region and the negative triboelectric field region, respectively, which were immediately adjacent to the pillar region. Subsequently, droplets of 0.1 M NaOH and HCl were released sequentially on the pre-charged module. The two droplets were observed to move in opposite directions and merge with the litmus, initiating a colorimetric reaction. This phenomenon was attributed to the fact that the 0.1 M NaOH was positively charged after CE with PTFE while the 0.1 M HCl was negatively charged. (Figure S28, Supporting Information). As shown in Figure 4f, droplet sorting could regulate the occurrence of reactions when the litmus droplet was positioned only in the positive triboelectric field region. The 10^{-3} M HCl droplet was found to be positively charged after sliding off the pre-charged module, contrary to the negatively charged 0.1 M HCl droplet. The negative charge on the 0.1 M HCl droplet after CE is likely due to H^+ adsorption on the PTFE surface. A 10^{-3} M HCl droplet slid off the pre-charged module and moved toward the negative triboelectric field region without reacting, whereas a 0.1 M HCl droplet was driven into the positive triboelectric field region and reacted with litmus (Movie S6, Supporting Information).

Ionic logic circuits utilize ions as carriers to transmit signals, offering the potential to control charge flux and regulate the direction and magnitude of ion currents akin to neural systems, amplifying signals, and operating at high frequencies.^[52,53] One can envision droplets as carriers for energy and information transfer in logic circuits, potentially controlling the leg-lifting direction in robots, etc. To enable this scenario, the size of the functional module was reduced to 5 cm \times 5 cm to demonstrate the capability of manipulating droplets without being limited by the size of the module. The micrometer-sized pillar region, positive triboelectric field region, and negative triboelectric field region were constructed according to the previous method. As shown in Figure 4g, two Al films (5 cm \times 0.5 cm) were pasted on each of the two triboelectric field regions immediately adjacent to the micrometer-sized pillar region for charge collection. In the absence of droplet movement, the circuit remained in an open state. The 10^{-5} M [EMIM]Cl droplets exhibited positive charges after passing through the pre-charged module. These droplets were attracted to the negative triboelectric field region, completing the external circuit and outputting a high-level signal to lift the robot's right leg. Subsequently, replacing the droplet with 0.1 M [EMIM]Cl, which carried a negative charge from CE, resulted in the droplet moving to the positive triboelectric field region, generating a reverse signal to lift the robot's left leg (Movie S7,

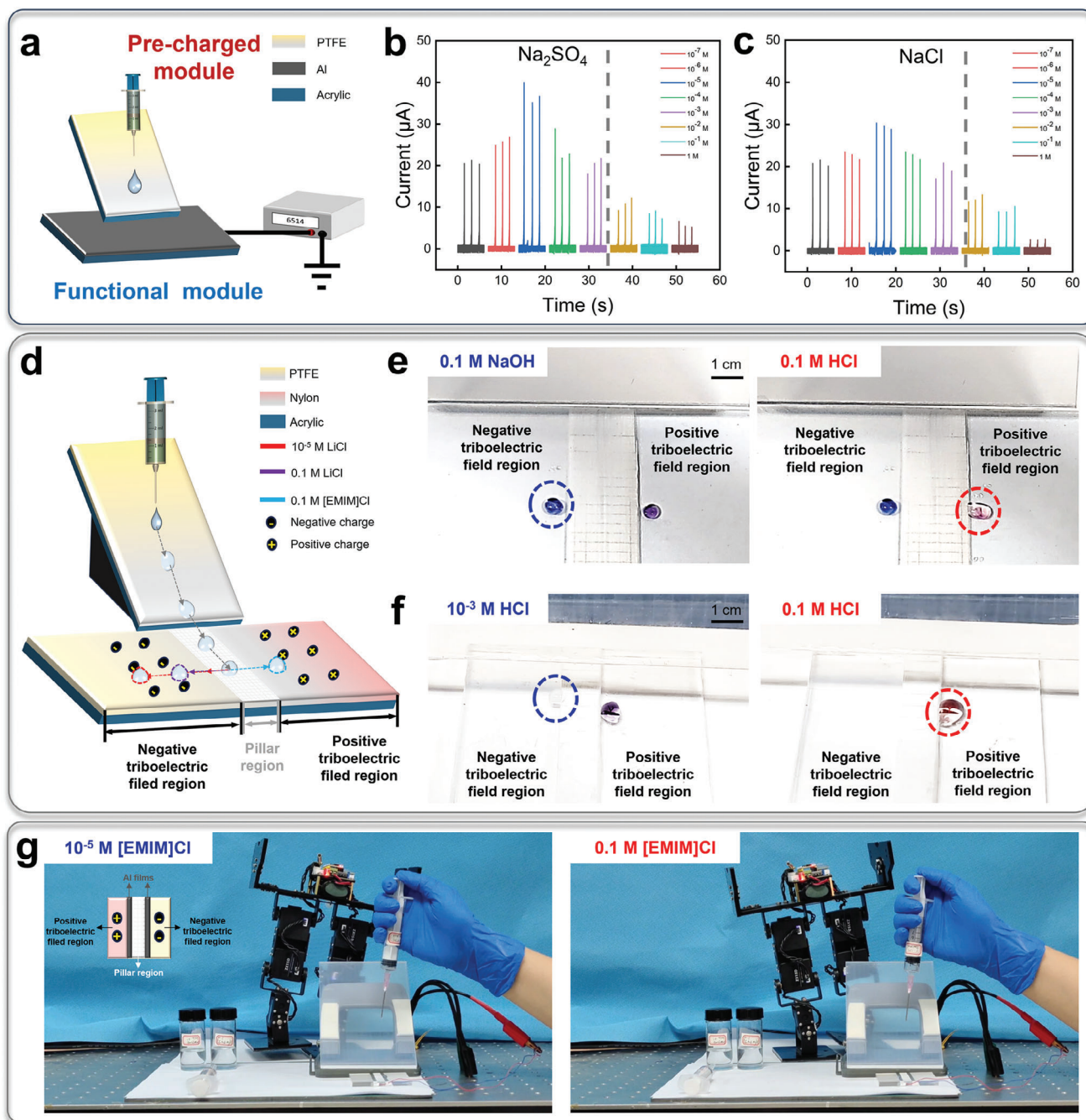


Figure 4. Triboelectric droplet manipulation and its applications. a) Schematic diagram of a modular chemical concentration detection device. b) Testing the range of the Na_2SO_4 content in droplets. c) Testing the range of the NaCl content in droplets. d) Schematic diagram of droplet sorting or chemical reaction modulation. e) Image showing droplets as reactors that can be transported in different directions for chemical reaction. f) Image showing droplet manipulation to control whether a chemical reaction occurs or not. g) Droplet manipulation enabled the regulation of ionic logic circuits thereby controlling the robot's leg lifting direction.

Supporting Information). This triboelectric droplet manipulation achieved logic control functions without the need for complex external power and electronic circuits. Overall, this study illustrates that a range of methods, whether remote or surface-based, dynamic or static, enable efficient droplet manipulation, demonstrating the adaptability and versatility of the approach.

3. Conclusion

In summary, a plug-and-play droplet manipulation paradigm based on triboelectrification and triboelectric-wetting on dielectric was proposed for flexible control of droplet motion on general dielectric surfaces. This approach integrated the triboelectric

charge from CE of S-S and L-S to govern droplet behavior through dynamical regulation of the EDL via asymmetric ion dynamics and electrostatic induction. The study revealed that the asymmetry of anions and cations in ionic liquids impacted the EDL at the L-S interface, directly influencing the triboelectric charge polarity and thereby controlling droplet motion. Compared to conventional EWOD methods, the droplet manipulation strategy based on EDL regulation exhibited superior collective performance in terms of no need for programmed path reconfiguration, reduced surface and energy constraints, antigravity capability, and flexibility. This strategy not only supported remote and in situ motion control from the droplet perspective without frequent predefined paths but also achieved a maximum average velocity of 450 mm s^{-1} on the common dielectric surface without chemical modifications, multiple-fold higher than the speeds observed in droplets subjected to constant electrostatic fields with modifications. Additionally, the modular manipulation strategy effectively decoupled the functionality, thus simplifying the complexity of the platform. Currently, the method does not incorporate superhydrophobic surface treatment, and the transport distance achieved is not the maximum reported. This will be the direction of our further research in the future. The adaptable plug-and-play strategy proved effective for ion concentration detection, chemical reaction modulation, and ionic logic circuit control. The use of dynamical regulation of EDL for droplet control introduced a novel paradigm for programmed manipulation, with significant potential for chemical analysis and self-powered smart sensing.

4. Experimental Section

Fabrication: Lithium chloride (LiCl) ($\geq 99\%$) was purchased from Aladdin, while 1-Ethyl-3-methylimidazolium Chloride ([EMIM]Cl) (98%) was purchased from Aladdin litmus reagent ($1\% \pm 0.05\%$). Polytetrafluoroethylene (PTFE) (99%, thickness $80 \mu\text{m}$), aluminum films (thickness 0.2 mm), acrylic (thickness 5 mm), and laboratory-prepared deionized water were purchased from the local market. Syringes were purchased from local pharmacies. The surface of the PTFE film was microscopically engraved by a laser engraving machine (Speedy 300, Trotec, Marchtrenk, Austria), and the laser had a power of 4 W and an engraving speed of 1 cm s^{-1} . The length and width of the constructed micrometer-scale structures were set to $100 \mu\text{m}$.

Characterization: The charge of the droplets was tested using an electrometer (6514, Keithley, Cleveland, OH, USA) and a Faraday cylinder. Real-time data collection was achieved using a platform built on a data acquisition card (BNC-2120, National Instruments, Austin, TX, USA) and Lab-View software. The topographical features of the samples were observed using a scanning electron microscope and the surface chemical composition was analyzed by EDS. Water's static contact angles were determined using a DSA-100 optical CA meter (Kruss Company, Ltd., Germany) with a test temperature set at room temperature.

Supporting Information

Supporting Information is available from the Wiley Online Library or from the author.

Acknowledgements

R.L. and X.L. contributed equally to this work. The authors are grateful for the support received from the National Natural Science Foundation

(Grant No. 22479016) and appreciate the technical assistance from the instrument & equipment platform of the Beijing Institute of Nanoenergy and Nanosystems. In addition, The authors thank Feiyao Yang, Yan Du, and Shaoxin Li from the Beijing Institute of Nanoenergy and Nanosystems for their help in checking the manuscript, building experimental platforms, and shooting demonstration videos.

Conflict of Interest

The authors declare no conflict of interest.

Data Availability Statement

The data that support the findings of this study are available in the supplementary material of this article.

Keywords

contact electrification, droplet manipulation, electrical double layer, plug-and-play, triboelectric-wetting

Received: September 4, 2024

Revised: September 28, 2024

Published online:

- [1] J. Ju, H. Bai, Y. Zheng, T. Zhao, R. Fang, L. Jiang, *Nat. Commun.* **2012**, *3*, 1247.
- [2] R. Yan, T. S. McClure, I. H. Jasim, A. K. R. Koppula, S. Wang, M. Almasri, C.-L. Chen, *Appl. Phys. Lett.* **2018**, *113*, 204101.
- [3] G. Chen, X. Liu, S. Li, M. Dong, D. Jiang, *Lab Chip* **2018**, *18*, 1026.
- [4] S. Högnadóttir, K. Kristinnsson, H. G. Thormar, K. Leosson, *Appl. Phys. Lett.* **2020**, *116*, 073702.
- [5] I. Oh, H. Cha, J. Chen, S. Chavan, H. Kong, N. Miljkovic, Y. Hu, *ACS Nano* **2020**, *14*, 13367.
- [6] M. Liu, J. Li, X. Zhou, J. Li, S. Feng, Y. Cheng, S. Wang, Z. Wang, *Adv. Mater.* **2020**, *32*, 1907999.
- [7] W. Li, Z. Wang, F. Yang, T. Alam, M. Jiang, X. Qu, F. Kong, A. S. Khan, M. Liu, M. Alwazzan, Y. Tong, C. Li, *Adv. Mater.* **2020**, *32*, 1905117.
- [8] W. Xu, H. Zheng, Y. Liu, X. Zhou, C. Zhang, Y. Song, X. Deng, M. Leung, Z. Yang, R. X. Xu, Z. L. Wang, X. C. Zeng, Z. Wang, *Nature* **2020**, *578*, 392.
- [9] X. Liu, H. Gao, J. E. Ward, X. Liu, B. Yin, T. Fu, J. Chen, D. R. Lovley, J. Yao, *Nature* **2020**, *578*, 550.
- [10] G. Kim, W. Kim, H. Chun, *Adv. Funct. Mater.* **2021**, *31*, 2105233.
- [11] H. Mertaniemi, R. Forchheimer, O. Ikkala, R. H. A. Ras, *Adv. Mater.* **2012**, *24*, 5738.
- [12] A. C. Sun, D. J. Steyer, A. R. Allen, E. M. Payne, R. T. Kennedy, C. R. J. Stephenson, *Nat. Commun.* **2020**, *11*, 6202.
- [13] J. Wang, T. Lu, M. Yang, D. Sun, Y. Xia, T. Wang, *Sci. Adv.* **2019**, *5*, eaau8769.
- [14] R. Malinowski, I. P. Parkin, G. Volpe, *Chem. Soc. Rev.* **2020**, *49*, 7879.
- [15] L. Yang, F. Yang, X. Liu, K. Li, Y. Zhou, Y. Wang, T. Yu, M. Zhong, X. Xu, L. Zhang, W. Shen, D. Wei, *Proc. Natl. Acad. Sci. U.S.A.* **2021**, *118*, 2023164118.
- [16] T. M. Schutzius, S. Jung, T. Maitra, G. Graeber, M. Köhme, D. Poulikakos, *Nature* **2015**, *527*, 82.
- [17] J. Li, J. Li, J. Sun, S. Feng, Z. Wang, *Adv. Mater.* **2019**, *31*, 1806501.
- [18] J. Nie, Z. Ren, J. Shao, C. Deng, L. Xu, X. Chen, M. Li, Z. L. Wang, *ACS Nano* **2018**, *12*, 1491.
- [19] J. Li, N. S. Ha, T. L. Liu, R. M. van Dam, C.-J. Kim, *Nature* **2019**, *572*, 507.

- [20] V. G. Venkata, T. R. Orth, W. Pan, A. Amini, G. M. Homsy, T. Liu, *Adv. Funct. Mater.* **2023**, *33*, 2301072.
- [21] J.-L. Zhu, W.-Y. Shi, T.-S. Wang, L. Feng, *Appl. Phys. Lett.* **2020**, *116*, 243703.
- [22] Y. Xiao, S. Zarghami, K. Wagner, P. Wagner, K. C. Gordon, L. Florea, D. Diamond, D. L. Officer, *Adv. Mater.* **2018**, *30*, 1801821.
- [23] A. Li, H. Li, Z. Li, Z. Zhao, K. Li, M. Li, Y. Song, *Sci. Adv.* **2020**, *6*, eaay5808.
- [24] Y. Huang, G. Wen, Y. Fan, M. He, W. Sun, X. Tian, S. Huang, *ACS Nano* **2024**, *18*, 6359.
- [25] Y. Jin, C. Wu, P. Sun, M. Wang, M. Cui, C. Zhang, Z. Wang, *Droplet* **2022**, *1*, 92.
- [26] H. Shen, H. Lei, M. Gu, S. Miao, Z. Gao, X. Sun, L. Sun, G. Chen, H. Huang, L. Chen, Z. Wen, *Adv. Funct. Mater.* **2022**, *32*, 2204525.
- [27] X. Dai, J. Yang, C. Shu, Q. Liang, J. Han, Y. Wu, M. Chen, Y. Cao, X. Ju, H. Sun, L.-B. Huang, G. Zhou, *Small* **2024**, *20*, 2310359.
- [28] J. Tan, Z. Fan, M. Zhou, T. Liu, S. Sun, G. Chen, Y. Song, Z. Wang, D. Jiang, *Adv. Mater.* **2024**, *36*, 2314346.
- [29] W. Xu, Y. Jin, W. Li, Y. Song, S. Gao, B. Zhang, L. Wang, M. Cui, X. Yan, Z. Wang, *Sci. Adv.* **2022**, *8*, eade2085.
- [30] H. Dai, C. Gao, J. Sun, C. Li, N. Li, L. Wu, Z. Dong, L. Jiang, *Adv. Mater.* **2019**, *31*, 1905449.
- [31] Y. Jin, W. Xu, H. Zhang, R. Li, J. Sun, S. Yang, M. Liu, H. Mao, Z. Wang, *Proc. Natl. Acad. Sci. U.S.A.* **2022**, *119*, 2105459119.
- [32] Q. Sun, D. Wang, Y. Li, J. Zhang, S. Ye, J. Cui, L. Chen, Z. Wang, H.-J. Butt, D. Vollmer, X. Deng, *Nat. Mater.* **2019**, *18*, 936.
- [33] Y. Jin, X. Liu, W. Xu, P. Sun, S. Huang, S. Yang, X. Yang, Q. Wang, R. H. W. Lam, R. Li, Z. Wang, *ACS Nano* **2023**, *17*, 10713.
- [34] Y. Jin, S. Yang, M. Sun, S. Gao, Y. Cheng, C. Wu, Z. Xu, Y. Guo, W. Xu, X. Gao, S. Wang, B. Huang, Z. Wang, *Nat. Commun.* **2024**, *15*, 4762.
- [35] X. Li, L. Zhang, Y. Feng, Y. Zhang, H. Xu, F. Zhou, D. Wang, *ACS Nano* **2023**, *17*, 23977.
- [36] X. Li, P. Bista, A. Z. Stetten, H. Bonart, M. T. Schür, S. Hardt, F. Bodziony, H. Marschall, A. Saal, X. Deng, R. Berger, S. A. L. Weber, H.-J. Butt, *Nat. Phys.* **2022**, *18*, 713.
- [37] D. Choi, H. Lee, D. J. Im, I. S. Kang, G. Lim, D. S. Kim, K. H. Kang, *Sci. Rep.* **2013**, *3*, 2037.
- [38] H. Mertaniemi, V. Jokinen, L. Sainiemi, S. Franssila, A. Marmur, O. Ikkala, R. H. A. Ras, *Adv. Mater.* **2011**, *23*, 2911.
- [39] H. Dai, Z. Dong, L. Jiang, *Sci. Adv.* **2020**, *6*, eabb5528.
- [40] L. Tan, Q. Zeng, F. Xu, Q. Zhao, A. Chen, T. Wang, X. Tao, Y. Yang, X. Wang, *Adv. Mater.* **2024**, *36*, 2313878.
- [41] W. Wang, H. Vahabi, A. Taassob, S. Pillai, A. K. Kota, *Adv. Sci.* **2024**, *11*, 2308101.
- [42] J. Sun, L. Zhang, S. Gong, J. Chen, H. Guo, *Adv. Mater.* **2023**, *35*, 2305578.
- [43] Y. Li, Y. Luo, S. Xiao, C. Zhang, C. Pan, F. Zeng, Z. Cui, B. Huang, J. Tang, T. Shao, X. Zhang, J. Xiong, Z. L. Wang, *Nat. Commun.* **2024**, *15*, 6004.
- [44] S. Lin, L. Xu, A. Chi Wang, Z. L. Wang, *Nat. Commun.* **2020**, *11*, 399.
- [45] D. Yoo, S. Jang, S. Cho, D. Choi, D. S. Kim, *Adv. Mater.* **2023**, *35*, 2370183.
- [46] J. Nie, Z. Ren, L. Xu, S. Lin, F. Zhan, X. Chen, Z. L. Wang, *Adv. Mater.* **2020**, *32*, 1905696.
- [47] A. Martín-Molina, C. Calero, J. Faraudo, M. Quesada-Pérez, A. Travesset, R. Hidalgo-Álvarez, *Soft Matter* **2009**, *5*, 1350.
- [48] Z. Tang, D. Yang, H. Guo, S. Lin, Z. L. Wang, *Adv. Mater.* **2024**, *36*, 2400451.
- [49] X. Li, S. Li, X. Guo, J. Shao, Z. L. Wang, D. Wei, *Matter* **2023**, *6*, 3912.
- [50] L. Limat, *Eur Phys J Spec Top* **2020**, *229*, 1833.
- [51] B. Andreotti, J. H. Snoeijer, *Annu. Rev. Fluid Mech* **2020**, *52*, 285.
- [52] H. Qian, D. Wei, Z. Wang, *Nano Res.* **2023**, *16*, 11718.
- [53] S. Li, Z. Zhang, F. Yang, X. Li, P. Peng, Y. Du, Q. Zeng, M. Willatzen, Z. L. Wang, D. Wei, *Device* **2024**, *2*, 100332.